



Reconstruction of the Regional Response of a Bridge Deck Based on Finite-Element Analysis

Weimin Zhang¹ · Xiayi Zheng² · Kan Liu³ · Jian Chen⁴

Received: 9 March 2023 / Revised: 24 June 2023 / Accepted: 16 August 2023 / Published online: 14 September 2023
© Krishtel eMaging Solutions Private Limited 2023, corrected publication 2023

Abstract

Purpose Bridges play a crucial role in ensuring regional connectivity and traffic safety. However, their vulnerability to environmental factors and material degradation can lead to varying degrees of damage. The bridge structural health monitoring system (SHMS) has emerged as an efficient and intelligent alternative to traditional detection methods to tackle these challenges.

Methods This paper presents an improved approach for reconstructing the response of measuring points based on proper orthogonal decomposition. First, the novel sensor layout scheme based on orthogonal decomposition is introduced to reconstruct stress responses at measuring points. Subsequently, the proposed response reconstruction theory is developed by decomposing stress responses from known points into random time functions and modes. These components are then combined with verification point modes and random time functions using the interpolation method, enabling the determination of stress responses at verification points. Lastly, the proposed response reconstruction theory is validated through numerical simulations and laboratory experiments.

Results The results demonstrate that the proposed method achieves an error rate of less than 5% when comparing the maximum stress response identified by the proposed method to the actual value. Moreover, it has minimal impact on vehicle weight, speed, and complex load factors.

Conclusion Therefore, the response reconstruction method and sensor layout scheme proposed in this study provide an accurate and efficient solution for bridge SHMS.

Keywords Proper orthogonal decomposition · Response reconstruction theory · Sensor layout scheme · Numerical simulation · Experiment verification

List of Symbols

L	Length of bridge
R	Covariance matrix
$E(m)$	Energy contained in the first m orders
D_j	Distance from the measurement point to the j_{th} prediction point
x_i, y_i	Location of the i_{th} measuring point
$\varepsilon(t)$	Strain–time–history response
$\varepsilon'(x, y, t)$	Strain response of the verification point (x, y)

$\varepsilon(x_i, y_i, t)$	Strain–time–history response at the i_{th} measuring point
$\varepsilon_{i,j}$	Stress–time–history response of the point $g_{i,j}$
$\varepsilon'_{i,k}$	Calibrated predicted stress response of the verification point $u_{i,k}$
$\varepsilon_{i,k}$	Predicted stress–time–history response of the verification point $u_{i,k}$
$\varepsilon''_{i,k}$	Stress response of the verification point corresponding operating condition of the FE model
$\varepsilon'''_{i,k}$	Revised response of the verification point
ϕ	Eigenmatrix
ϕ_n	Basis vector on the n_{th} axis of the orthogonal coordinate
$\phi_n(x_i, y_i)$	The value of the eigenmode ϕ_n at the measuring point (x_i, y_i)
$\phi'_n(x, y)$	Approximate eigenmode values of the verification point (x, y)

✉ Jian Chen
z20120160201@zjtongji.edu.cn

¹ Jinhua Polytechnic, Jinhua, China

² Hangzhou Jianyan Technology Co. Ltd, Hangzhou, China

³ Sichuan University, Chengdu, China

⁴ Zhejiang Tongji Vocational College of Science and Technology, Hangzhou, China

$\phi_n(x_j, y_j)$	The eigenmode values of the measurement points (x_j, y_j)
$\phi'(u_{i,k})$	The eigenmode of the k_{th} verification point
$\phi'(g_{i,j})$	The eigenmode of the j_{th} known point
a_j	Distance of the j_{th} known point $g_{i,j}$ from the leftmost support
a_n	Projection of the strain response vector on the n_{th} axis
$a'_n(t)$	Approximate principal coordinates
$a_n^2(t)$	Root mean square value of the principal coordinates
$r_{i,j}$	Ratio of the j_{th} known point on the i_{th} main beam
$r_{i,k}$	Ratio of the k_{th} verification point $u_{i,k}$
$r'_{i,k}$	Response ratio of the k_{th} verification point $u_{i,k}$
$f_{i,k}$	Calibration curve of the verification point $u_{i,k}$
$IL_{i,j}$	Value of influence line on the known point $g_{i,j}$
$IL_{i,k}$	Value of the influence line on the verification point $u_{i,k}$
$M_{i,j}$	Maximum value of $IL_{i,j}$
$\beta_{i,k}$	Criterion for determining the validity of the reconstructed response for the verification point
δ_{mn}	Kronecker symbol
$\eta_{i,k}$	Distribution of the calibrated predicted stress response ratios for the verification point $u_{i,k}$
$\eta'_{i,k}$	Calibration curve of the verification point $u_{i,k}$ of the FE model.
λ_n	Constant value
$\lambda_{i,k}$	Maximum calibration coefficient of the verification point $u_{i,k}$
v_m	Speed of the test trolley
v_r	Speed of the finite-element simulated vehicle
l_m	Length of test bridge
l_r	Length of the finite-element model bridge
F	Frequency of the motor
v	Speed of the car
l	Perimeter of the rotating shaft

Introduction

The development of regional economies and national security is closely intertwined with the improvement of transportation infrastructure, with bridges playing a crucial role. Monitoring the overall response of large-span bridge structures and conducting regular health and safety assessments are essential. The structural health monitoring system encompasses various components, including the sensing system, signal transmission and storage system, structural condition parameter identification, damage identification based on monitoring data, and structural performance evaluation. Among these components, the sensing system stands as the fundamental cornerstone of the entire

structural health monitoring system. In recent years, a multitude of innovative sensing technologies have emerged, such as optical fiber sensing methods [1–3] and wireless sensing means [4, 5]. These advanced sensing technologies are increasingly employed in the health monitoring process of bridges due to their notable stability and adaptability to varying environmental conditions.

As a typical large span and complex structure, a significant number of sensing devices are required to capture the full response of the bridge. The wired sensors require numerous wires for data transfer, resulting in increased monitoring system costs. In addition, it is impractical to install sensors in all degrees of freedom of the bridge. Optimizing the arrangement of sensors and monitoring methods has proved to be a challenging issue, prompting lots of researchers to conduct relevant research [6]. A variety of optimization criteria and computational methods have been developed to achieve optimal sensor placement based on modal observability. These methods predominantly rely on various modal parameters, including the minimization of transfer errors [7], energy-based criteria [8], model reduction criteria [9], and modal assurance criteria [10]. Another approach to sensor placement optimization involves focusing on damage recognizability, whereby sensors are positioned at locations that exhibit high sensitivity to structural damage, allowing the resulting performance matrix of structural responses to contain comprehensive information about the damage. However, research on sensor optimization with damage recognition as the objective remains relatively limited [11]. In other methods, sensors are typically allocated to surface nodes corresponding to the structural system and finite-element analysis, resulting in an integer programming problem for combined optimization. The effective independence method [7] and the successive reduce method [12] are commonly employed techniques for this purpose. In addition, the economy of the surveillance system is an important factor to consider. Zhang et al. [13] introduced a method that simultaneously detects damage and vehicle loads on simply supported girder bridges. The long-spaced fiber Bragg grating (FBG) sensors is utilized to reducing the number of devices required while maintaining accurate identification results with less cost. Furthermore, Zhang et al. [14] explored the application of long-range FBG sensors for damage identification in highway bridges, observing their high resistance to noise and suitability for uninterrupted and long-term monitoring. Similarly, Chen et al. [15] proposed a detection method that employs a long-range fiber-optic grating sensor to identify both the location and extent of bridge damage, even under conditions of random vehicular traffic flow.

Apart from optimizing the number of sensors, the acquisition of bridge parameters with a limited number of sensors is an important area of research. Numerous methods proposed by researchers have proposed, including the technique of structural dynamic response reconstruction. This technique decomposes the data measured by the sensors into modal

and random time functions. By combining the calculated modal data with the random time function, the response at the measurement points can be reconstructed. As a result, this approach compensates for the limited measurement data by providing comprehensive structural response information using fewer sensors, reducing economic costs. The structural dynamic response reconstruction is mainly divided into three methods based on modal analysis [16–19], transmissibility [20] and Markov parameter [21]. In 1997, Kammer [22] first proposed the concept of structural dynamic response reconstruction method, using the measured responses of other positions on the structure to predict the response of discrete unidentified positions. A transformation matrix based on Markov parameters was proposed to convert the information collected by the sensor into the response of the desired position. He [23] presented a dynamic response reconstruction method based on empirical mode decomposition (EMD) [24–26]. Ribeiro [27] presented a transfer rate matrix for multi-degree of freedom systems. This matrix was effectively employed to determine the position response of an unknown reconstructed structure, assuming the prior knowledge of excitation force position. According to the above displacement transfer matrix, Law [28] expanded it into acceleration transfer matrix, considered the influence of sampling time, sampling rate, number of sensors and measurement noise on formula parameters. Wang [29] applied Markov parameter matrix in response reconstruction, converted Markov parameter matrix into full rank matrix by Jacobi transform and QR decomposition, and optimized sensor layout by constructing objective function based on reducing noise influence.

The proper orthogonal decomposition (POD) method, also known as the Karhunen–Loeve theorem, has been widely applied for response reconstruction. MA [30] utilized the lower order modes obtained from Karhunen–Loeve decomposition to reconstruct the response of a truss structure, revealing that the first few modes captured the overall structural information. Bienkiewicz [31] performed POD decomposition on the pulsating wind pressure of a large-span flat-top low-rise building, reconstructing the roof wind pressure field using the dominant modes and verifying the effectiveness of the reconstruction. Ni [32] employed the inverse distance weighting method to interpolate the eigenmodes of predicted points based on the eigenmode values obtained from wind tunnel tests, and calculated the wind pressure at these points using the time series of predicted point positions decomposed by the POD method. Jiang [32] conducted a wind tunnel test on a double-slope roof using a synchronous method. However, it can be found that the prior research on response recognition has predominantly focused on one-dimensional structures, neglecting the two-dimensional nature of bridge decks, which encompasses both

transverse and longitudinal areas. To overcome this limitation, this study introduces an improved response reconstruction method based on the principle of proper orthogonal decomposition.

The paper is organized as follows: “**Introduction**” introduces the current research on bridge response reconstruction and the optimization of wireless sensor placement in bridge health monitoring. “**Response Reconstruction Theory of the Bridge Based on POD Method**” presents the theoretical basis of bridge response reconstruction using POD method. Section 3 compares the finite-element numerical method with theoretical results using a real bridge as an example. “**Experimental Verification**” analyzes the practical accuracy of the theoretical approach by developing a simplified model of a multi-span bridge in the laboratory. Finally, “**Conclusions**” provides a summary of the overall findings of the paper.

Response Reconstruction Theory of the Bridge Based on POD Method

Fundamental Principle of Proper Orthogonal Decomposition

The POD method, which effectively characterizes the wind pressure field on the surface of the structure, reconstructs the field using a limited number of first eigenmodes while disregarding higher order covariance modes [34]. The POD method has been commonly employed in studying wind loads on buildings [35, 36], analyzing wind-induced responses [37], reconstructing wind pressure fields [38, 39], conducting wind tunnel tests [40], and model order reduction [41]. Various approaches have been utilized to establish the POD principle [42], such as the Karhunen–Loeve decomposition theorem, Tamura and Bienkiewicz’s projection extreme value principle, the Lagrange multiplier method, and the Rayleigh quotient concept in structural dynamics. In this study, the POD principle is derived from the Rayleigh quotient concept in structural dynamics and applied to identify the strain response of bridge structures.

It is assumed that the strain vector $\varepsilon(t)$ represents the strains of N measuring points on the model surface, obtained from the dynamic experiment conducted on the bridge. This is illustrated as follows:

$$\varepsilon(t) = \{\varepsilon_1(t), \varepsilon_2(t), \dots, \varepsilon_N(t)\}^T \quad (1)$$

where $\varepsilon_i(t) = \varepsilon(x_i, y_i, t)$ is the strain–time–history response of the i_{th} measuring point located at (x_i, y_i) .

Consider ϕ_n as the basis vector along the n_{th} axis of the orthogonal coordinate system, and $a_n(t)$ as the principal coordinate, representing a random time function. The projection of the strain response vector onto this axis is denoted as $a_n(t)$, and can be expressed as

$$a_n(t) = \varepsilon(t)^T \phi_n = \phi_n^T \varepsilon(t), \quad (n = 1, 2 \dots N) \quad (2)$$

To maximize the projection of positive and negative stress, the mean square method is commonly used by regularizing Eq. (2) and it can be written as

$$\overline{a_n^2(t)} = \frac{\overline{\phi_n^T \varepsilon(t) \varepsilon(t)^T \phi_n}}{\overline{\phi_n^T \phi_n}} = \frac{\phi_n^T R \phi_n}{\phi_n^T \phi_n} = \lambda_n \quad (3)$$

where $\overline{a_n^2(t)}$ represents the mean square value of the principal coordinate; R is the covariance matrix; λ_n is the constant value involved in the equation.

The Rayleigh quotient problem involves determining the value of vector ϕ_n when λ_n reaches its maximum. Based on the extreme value property of the Rayleigh quotient, a stationary value can be obtained from Eq. (3) using the eigenvector of the covariance matrix R . ϕ_n is an eigenvector of R , the mean square value $\overline{a_n^2(t)}$ reaches a stationary point equal to the eigenvalue λ_n of the covariance matrix R . Therefore, the relationship between them can be expressed as

$$R\phi_n = \lambda_n \phi_n, \quad (n = 1, 2 \dots N) \quad (4)$$

It is assumed that the eigenvectors have been regularized. The eigenmatrix ϕ and the principal coordinate vector $a(t)$ are defined as

$$\begin{cases} \phi = \{\phi_1, \phi_2, \dots, \phi_N\} \\ a(t) = \{a_1(t), a_2(t), \dots, a_N(t)\}^T \end{cases} \quad (5)$$

Then, Eq. (2) can be rewritten as

$$a(t) = \phi^T \varepsilon(t) \quad (6)$$

The orthogonality of the eigenmatrix ϕ can be obtained from the equations mentioned above, as shown in Eq. (7).

$$\varepsilon(t) = \phi a(t) = \sum_{n=1}^N a_n(t) \phi_n \quad (7)$$

The response expression for strain–time history at the i_{th} measurement point is, therefore, written as Eq. (8):

$$\varepsilon(x_i, y_i, t) = \varepsilon_i(t) = \sum_{n=1}^N a_n(t) \phi_n(x_i, y_i) \quad (8)$$

where $\phi_n(x_i, y_i)$ is value of the intrinsic mode at the specific measurement point. Furthermore, it has been demonstrated that the principal coordinates exhibit orthogonality among themselves, which can be expressed as

$$\begin{aligned} \overline{a_m(t) a_n(t)} &= \overline{\phi_m^T \varepsilon(t) \varepsilon(t)^T \phi_n} \\ &= \phi_m^T R \phi_n \\ &= \lambda_m \delta_{mn} \end{aligned} \quad (9)$$

where δ_{mn} is the Kronecker symbol. Let $m = n$, then we have

$$\overline{a_n^2(t)} = \lambda_n \quad (10)$$

Moreover, it can be observed that

$$\overline{\varepsilon^2(x_i, y_i, t)} = \sum_{n=1}^N \lambda_n \phi_n^2(x_i, y_i) \quad (11)$$

The eigenvalue can be regard as the indicator of the eigenvector's contribution to the mean square value of the strain–time-history response. By arranging the eigenvalues in descending order, the initial m eigenmodes tend to possess a substantial amount of energy, which can be harnessed for strain field reconstruction and computational load reduction. The determination of m adheres to the equation presented as follows:

$$E(m) = \frac{\sum_{i=1}^m (\lambda_i)^2}{\sum_{i=1}^N (\lambda_i)^2} \quad (12)$$

where $E(m)$ is the energy contained within the eigenvectors, with a higher percentage indicating a greater amount of energy captured and a closer resemblance of the reconstructed strain field to the original state. For this study, the solution is determined by selecting m such that the energy contained reached 99%. Based on Eq. (8), the strain field can be reconstructed accordingly:

$$\varepsilon(x, y, t) = \sum_{n=1}^m a_n \phi_n(x, y) \quad (13)$$

Let $\varepsilon'(x, y, t)$ represent the strain response at the verification point (x, y) . According to the POD principle, the response can be expanded with the first m eigenmodes:

$$\varepsilon'(x, y, t) = \sum_{n=1}^m a'_n \phi'_n(x, y) \quad (14)$$

If the measuring points are uniformly arranged, the determination of principal coordinates and eigenmodes can be obtained based on Eqs. (15) and (16):

$$a'_n(t) = \frac{\sum_{i=1}^N \varepsilon(x_i, y_i, t) \phi_n(x_i, y_i)}{\sum_{i=1}^N \phi_n^2(x_i, y_i)} \quad (15)$$

$$\phi'_n(x, y) = \frac{\sum_{j=1}^k \frac{1}{(D_j)^p} \phi_n(x_j, y_j)}{\sum_{j=1}^k \frac{1}{(D_j)^p}} \quad (16)$$

where $a'_n(t)$ is the approximate principal coordinate; (x_j, y_j) refers to the coordinates of the known point; $\phi'_n(x, y)$ is the approximate value of the intrinsic mode of the verification

point; $\phi_n(x_j, y_j)$ denotes the known intrinsic mode value at the surrounding measuring points. The number of measuring points involved in the calculation is at least 6, which means $k = 6$. D_j is the distance from the corresponding measuring point to the predicted point (x, y) ; p is the power of the distance, which is determined based on the minimum error criterion.

Hence, the POD method decomposes the measured point response into eigenmodes and random time functions. The point mode is then validated to reconstruct the response using the aforementioned formulation. Additionally, Eq. (16) is referred to as the inverse distance weighting method, which necessitates a minimum of six known points. However, acquiring the response of a verification point demands a substantial number of sensors, imposing position restrictions that are neither cost-effective nor practical in engineering applications. Moreover, this approach is time-consuming and energy-intensive.

To tackle the aforementioned challenges, we propose a sensor layout scheme to mitigate these concerns. By incorporating interpolation techniques based on modal characteristics, the verification point modes are obtained to facilitate response reconstruction. This innovative approach involves utilizing two known points to reconstruct the response of the measured points. Through modification of the formula derived from the binding force method and finite-element method, precise outcomes can be attained.

Response Reconstruction Combining with Force Method

Figure 1 illustrates the configuration of a multi-span bridge. To aid in explaining the proposed algorithm, we make the following assumptions. The bridge comprises s main girders, each consisting number of Q know points. On each main girder, there exist a set of known points denoted as $g_{i,j}$ and a set of validation points denoted as $u_{i,k}$. Here, the subscript i represents each main girder ($i = 1, \dots, s$), j indicates the j_{th} known point, and k denotes the k_{th} validation point.

The m -order eigenmodes presented for the known points, which capture the structural information, are written as Eq. (17):

$$\phi'_n = \{\phi'_n(g_{i,1}), \phi'_n(g_{i,2}), \dots, \phi'_n(g_{i,Q})\} \quad (n = 1, 2 \dots m) \quad (17)$$

Then, the eigenmode $\phi'(u_{i,k})$ of the verification point $u_{i,k}$ is expressed as

$$\phi'_n(u_{i,k}) = \frac{\phi'_n(g_{i,j}) + \phi'_n(g_{i,j+1})}{2} \quad (n = 1, 2 \dots m) \quad (18)$$

$$\begin{bmatrix} g_{i,1} & u_{i,1} & g_{i,2} & u_{i,2} & \dots & g_{i,j} & u_{i,k} & g_{i,j+1} & \dots & g_{i,Q-1} & u_{i,z} & g_{i,Q} \\ \vdots & \vdots & \vdots & \vdots & \ddots & \vdots & \vdots & \vdots & \ddots & \vdots & \vdots & \vdots \\ g_{i,1} & u_{i,1} & g_{i,2} & u_{i,2} & \dots & g_{i,j} & u_{i,k} & g_{i,j+1} & \dots & g_{i,Q-1} & u_{i,z} & g_{i,Q} \\ \vdots & \vdots & \vdots & \vdots & \ddots & \vdots & \vdots & \vdots & \ddots & \vdots & \vdots & \vdots \\ g_{s,1} & u_{s,1} & g_{s,2} & u_{s,2} & \dots & g_{s,j} & u_{s,k} & g_{s,j+1} & \dots & g_{s,Q-1} & u_{s,z} & g_{s,Q} \end{bmatrix}$$

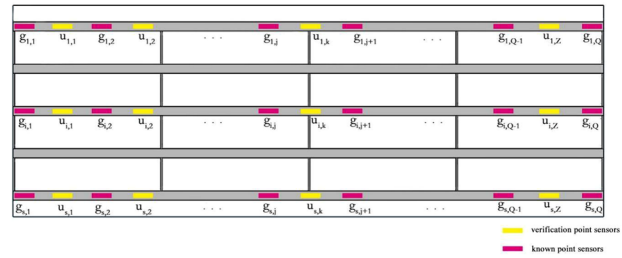


Fig. 1 The simulated arrangement of sensors at the bottom of the bridge

where $\phi'(u_{i,k})$ and $\phi'_n(g_{i,j})$ are the eigenmode of the k_{th} verification point and the $(j + 1)_{th}$ known point on the i_{th} main beam, respectively, ($i = 1, 2, \dots, s; j = 1, 2, \dots, Q; k = 1, 2, \dots, Z$).

Based on Eq. (14), the structural response can be determined using the eigenmodes and random time functions obtained from Eq. (18). The response obtained at the verification point is referred to as the predicted stress response, which may have limited accuracy. To improve the accuracy, a combination of mechanical methods and finite-element analysis is considered to modify the predicted stress response. This approach aims to establish a formulation for reconstructing the structural response and introduces the coefficient β based on the proportion distribution law to evaluate the results. The formulation of the influence line at any measuring point on a simply supported beam under a unit load can be expressed as follows:

$$IL_{i,j} = \begin{cases} \frac{x}{L}(L - a_j) & (0 \leq x \leq a_j) \\ [10pt] \frac{(L - x)a_j}{L} & (a_j \leq x \leq L) \end{cases} \quad (19)$$

where $IL_{i,j}$ represents the influence line of the j_{th} known point $g_{i,j}$ on the i_{th} section of the main beam; L is the total length of the bridge; a_j is the distance between the j_{th} known point on the i_{th} girder and the leftmost support.

The ratio $r_{i,j}$ is determined by comparing the maximum stress response at the known point with the maximum value of the corresponding the influence line of the measuring point, as expressed as follows:

$$r_{i,j} = \frac{\max(\epsilon_{i,j})}{M_{i,j}} \quad (20)$$

where $r_{i,j}$ and $\epsilon_{i,j}$ are the ratio and stress–time-history response of the j_{th} known point $g_{i,j}$ on the i_{th} section of the

main beam, respectively; $M_{i,j}$ is the maximum value of when the unit force acted. Therefore, the ratio $r_{i,k}$ of the verification points is written as

$$r_{i,k} = \frac{r_{i,j} + r_{i,j+1}}{2} \quad (21)$$

where $r_{i,k}$ and $r_{i,j+1}$ are the ratio of the k_{th} verification point $u_{i,k}$ and the $(j+1)_{\text{th}}$ known point $g_{i,j+1}$ on the i_{th} main beam, respectively. And the value of $r_{i,j}$ and $r_{i,j+1}$ can be obtained by Eq. (20).

The ratio $r'_{i,k}$ can be obtained by comparing the maximum value of the predicted stress response at the verification point with the influence line corresponding to the measurement point:

$$r'_{i,k} = \frac{\max(\varepsilon_{i,k})}{M_{i,k}} \quad (22)$$

where $r'_{i,k}$ and $\varepsilon_{i,k}$ are the predicted response ratio and the predicted stress–time–history response respect to the k_{th} verification point on the i_{th} main beam; $M_{i,k}$ is the maximum value of $IL_{i,k}$ when the unit force only acts on the k_{th} verification point $u_{i,k}$. After that, the maximum calibration coefficient λ for each verification point can be deduced from Eqs. (20) and (22):

$$\lambda_{i,k} = \frac{r_{i,k}}{r'_{i,k}} \quad (23)$$

where $\lambda_{i,k}$ is the maximum calibration coefficient of the k_{th} verification point $u_{i,k}$ on the i_{th} main beam.

The maximum calibration coefficient $\lambda_{i,k}$ of each verification point is taken as the peak value, and the time when the peak value occurs is when the load acts on the position of the verification point. A calibration curve $f_{i,k}$ can be obtained by linearly decreasing from the verification point towards the left and right ends. The predicted value of calibration stress response of verification point is

$$\varepsilon'_{i,k} = f_{i,k} \cdot \varepsilon_{i,k} \quad (24)$$

where $\varepsilon'_{i,k}$ and $f_{i,k}$ are the predicted stress response after calibration and the calibration curve of the k_{th} verification point $u_{i,k}$ on the i_{th} main beam, respectively. And $f_{i,k}$ is deduced linearly from the peak value to both ends according to the maximum calibration coefficient $\lambda_{i,k}$.

The aforementioned formulas serve to validate the initial calibration of the predicted structural response, while the effectiveness of the calibration results is evaluated through the coefficient of lateral proportional distribution law. A finite-element model is developed using parameters specific to the existing bridge, such as its length, width, material, section shape, and number of main beams. By simulating identical lane loading conditions, the stress–time–history

response $\varepsilon'_{i,k}$ is extracted for all verification points. For verification points located on the same cross-section, the proportion distribution law $\eta'_{i,k}$ is calculated using the following formula:

$$\eta'_{i,k} = \frac{\max(\varepsilon''_{i,k})}{\sum_{i=1}^s \max(\varepsilon''_{i,k})} \quad (25)$$

where $\eta'_{i,k}$ and $\varepsilon''_{i,k}$ are the calibration curve and the stress response of the k_{th} verification point $u_{i,k}$ of the i_{th} section of the finite-element model under corresponding working conditions.

Similarly, using the calibrated predicted stress response $\varepsilon'_{i,k}$ obtained from the first calibration, we can derive the proportional distribution law $\eta_{i,k}$ for the calibrated predicted response of verification points located on the same cross-section:

$$\eta_{i,k} = \frac{\max(\varepsilon'_{i,k})}{\sum_{i=1}^s \max(\varepsilon'_{i,k})} \quad (26)$$

where $\eta_{i,k}$ is the proportional distribution law of predicted stress response after calibration of the k_{th} verification point $u_{i,k}$.

Using Eq. (24), the response prediction value of the measuring point is calculated and the validity of the calculation result is assessed by the coefficient of lateral proportional distribution law. Therefore, the coefficient β can be obtained by combining Eqs. (25) and (26), as shown as follows:

$$\beta_{i,k} = \frac{\eta'_{i,k}}{\eta_{i,k}} \quad (27)$$

where $\beta_{i,k}$ is the basis for assessing the reconstruction response effectiveness of the k_{th} verification point of the i_{th} section main beam. If $\beta_{i,k} \approx 1$, it indicates that the calibrated predicted stress response $\varepsilon'_{i,k}$ at the verification point satisfies the desired accuracy and can be considered as the final reconstructed stress response. However, if $\beta_{i,k} \neq 1$, it suggests that further revision is needed for the verification point.

Taking the peak value β as the maximum calibration coefficient, it can be determined that the load is applied at the position of the verification point when the peak value occurs. Therefore, the calibration curve $f'_{i,k}$ is obtained, which decreases from the position of the verification point towards both ends. The revised response of the verification point is then expressed as follows:

$$\varepsilon'''_{i,k} = f'_{i,k} \cdot \varepsilon'_{i,k} \quad (28)$$

The Step for the Response Reconstruction of the Bridge

As mentioned in “Response Reconstruction Combining with Force Method” and “The Step for the Response Reconstruction of the Bridge”, the POD principle is applied to reconstruct and predict the structural response, incorporating the influence line formulation for simply supported beams. The stress response at the measurement points is then calibrated and predicted, and the coefficients of the scaled distribution law are determined by finite-element model analysis for secondary calibration. The combination of these evaluation methods improves the accuracy of the reconstructed measurement point responses and facilitates the identification of responses within the bridge area. Integrating the previous sections, the entire step is summarized as shown in Fig. 2.

In Finite-Element Numerical Simulation, the effectiveness of the proposed method is demonstrated using a real bridge as a case study. The results of the bridge measurement point response reconstruction method presented in this paper show high accuracy and validity over different bridge decks. The method successfully identifies the responses of all measurement points across the entire bridge deck, including both lateral and longitudinal directions. This enables the acquisition of comprehensive two-dimensional structural information through regional response reconstruction.


Finite-Element Numerical Simulation

Model Introduction

To investigate regional response reconstruction in bridges using long-gauge sensing methods, we simulate a T-shaped simply supported beam with a total length of 48 m using the finite-element method. The simply supported T-beam is constructed using C55 concrete, and the section of the main beam of the superstructure comprises five prestressed

T-beams. The single T-beam of the bridge has a height of 2.75 m and a width of 2.64 m, while the width of the entire bridge is 13.2 m, excluding the sidewalks and railings on both sides. The bridge is hinged on both ends. We employ the grillage method to establish the finite-element model of the bridge based on the given parameters, and virtual beam materials with zero capacity transversely connect the five T-beams.

The single T-beam of the bridge model is divided into 16 units, each spanning 3 m. The entire bridge model is composed of 80 units and 85 nodes. Diaphragms are positioned at 6 m intervals from the bridge support, with a height of 2.4 m calculated from the top plate of the T-beam flange, which has a thickness of 0.2 m. In total, there are 9 diaphragms, including those at both ends of the support and the middle. Figure 3 illustrates the cross-section of the model girder and the overall structure of the model.

The internal measurement points are selected as the verification points in the blue dotted line box in Fig. 4. A total of 20 verification points are obtained from the placement of 4 measurement points, distributed among the 5 beams. The bridge sensor layout scheme, illustrated in Fig. 4, depicts the placement of 25 long standard distance FBG sensors, represented by the red mark (“”).

Verification by Finite-Element Method

The purpose of the numerical simulation is to validate the effectiveness of the proposed method. For the sake of simplifying the verification process, a centralized moving load is employed to emulate the actual bridge crossing scenario. Specifically, a two-axle trolley with a total weight of 3 tons is simulated to traverse the bridge at a constant speed. The simulation involves applying a moving load to the middle No.3 main girder, with the trolley moving at a speed of $v = 3$ m/s. To represent the axle weights of the simplified two-axle trolley, two concentrated forces, $P1$ and $P2$, are utilized with a specific time interval. $P1$ is set to 10 kN, $P2$ is set to 20 kN,

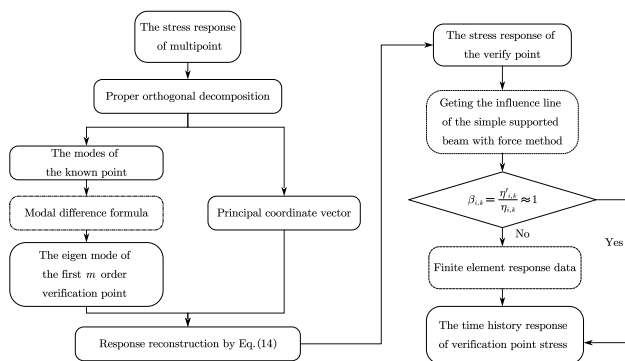


Fig. 2 The flowchart for the bridge’s response reconstruction based on POD method

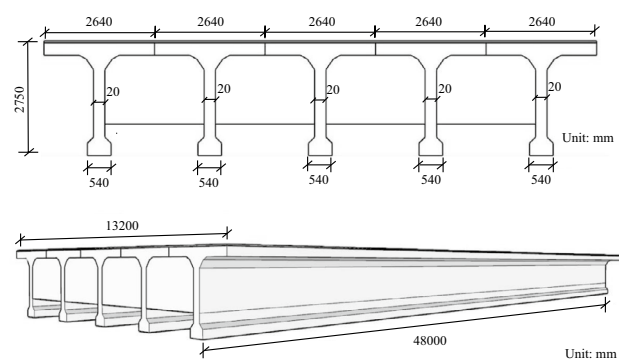


Fig. 3 The diagram of the overall structure of the model

and the wheelbase of the two-axle trolley is 3 m. This setup reflects a standard working condition, as shown in Fig. 5. Meanwhile, the stress response data from the sensor arrangement points depicted in Fig. 4 are collected for analysis and verification. It should be noted that the analysis takes into account the influence of 10% white noise.

The predicted stress response values (PV) obtained through POD, the actual stress response values (RV) and the optimal stress response values (OV) calculated using the proposed response method are compared across all verification points. For demonstration and comparison purposes, the verification points of No. 42 and No. 59 are selected, as depicted in Fig. 4. Therefore, the stress value of PV, RV and OV are obtained, as drawn in Fig. 6. The error diagrams for the remaining verification points are presented in the measurement points error diagram under standard working conditions.

In Fig. 6, the PV and RV curves exhibit the error, which is more pronounced at the peak, particularly for the measuring points on the middle main beam. In contrast, the OV curve

aligns closely with the RV curve for each validation point, showing a high level of agreement, except for a few distinct points. This demonstrates the effectiveness and accuracy of the proposed response reconstruction method in identifying all measurement points within the bridge deck area. Furthermore, to ensure consistency and avoid the influence of varying working conditions such as vehicle weight, speed, and load, the same verification points are selected for analyzing and comparing the results.

The effectiveness of the proposed method is evaluated under varying trolley weights to assess its performance in different working conditions. Specifically, the trolley load is adjusted to $P_1 = 30$ kN and $P_2 = 50$ kN, resulting in a total weight of 80 kN, while keeping the wheelbase and trolley speed constant. The same verification and reference points are selected as in the standard working conditions. Stress response data are collected from the sensor locations, accounting for 10% white noise, and the results are analyzed and verified. For comparison,

Fig. 4 The layout of verification points and the sensor in the bridge model

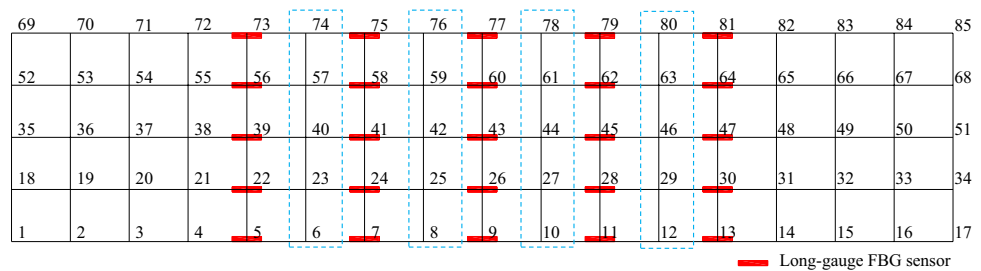


Fig. 5 Single carriageway moving load layout

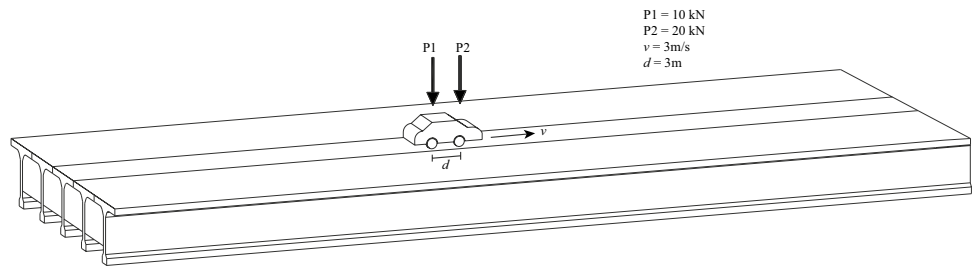
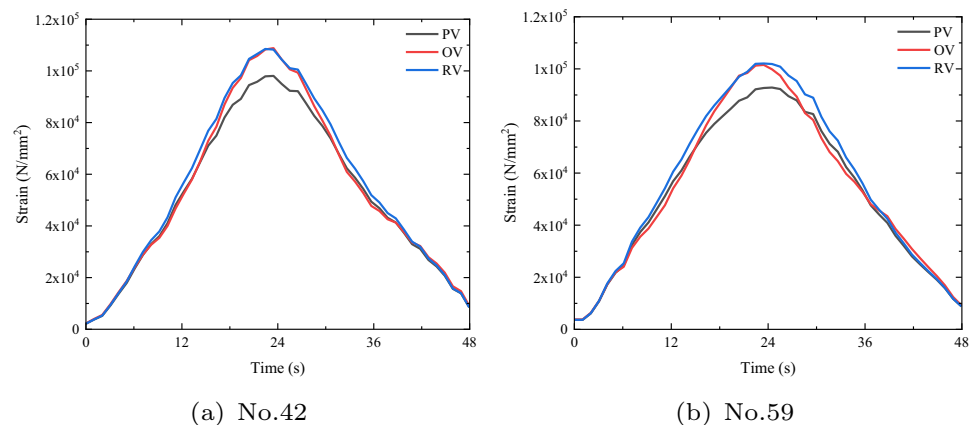


Fig. 6 Comparison of Measured Point Response



verification points No. 42 and No. 59 are chosen from all the verification points and displayed in Fig. 7. The error diagram of the measurement points under the vehicle load condition presents the results for the remaining verification points.

In addition to adjusting the trolley weight, the vehicle speed is another parameter that can impact the proposed response reconstruction method. In this study, the simulated vehicle speed is increased from $v = 3$ m/s to 4 m/s, while maintaining the small axle weight and wheelbase constant. The selection of verification points and known points remains the same as in the standard working conditions. Stress response data from the sensor locations are collected and analyzed, considering 10% white noise. The results for verification points No. 42 and No. 59, selected from all the verification points, are presented and compared in Fig. 8. The measuring point error of the vehicle speed shows the results for the remaining verification points. The comparison demonstrates the effective identification of all measurement points within the bridge deck

area and the accurate reconstruction of stress response values achieved by the proposed method.

A moving load, representing by a two-axle trolley, is applied to the two main beams of the bridge to simulate the scenario of two lanes traveling together. The combined weight of both cars is 3 tons. Car A has front and rear axles with a wheelbase of 3 m and a speed of $v_1 = 3$ m/s, with axle loads $P11=10$ kN and $P12 = 20$ kN, respectively. Car B also has front and rear axles with a wheelbase of 3 m and a speed of $v_2 = 3$ m/s, with axle loads $P21=10$ kN and $P22 =20$ kN, respectively. The driving lanes of the two cars are depicted in Fig. 9. The verification points of No. 42 and No. 59 are selected for comparison and displayed in Fig. 10, while the results for other verification points are presented in the measuring point error diagram under vehicle speed conditions.

When comparing the responses of measuring points under vehicle load, vehicle speed, and complex load conditions, a certain level of error is observed between the PV curve and RV curve. This error is particularly pronounced at the peak, with the measuring points on the middle girder

Fig. 7 Comparison of the measurement point response considering the vehicle load condition

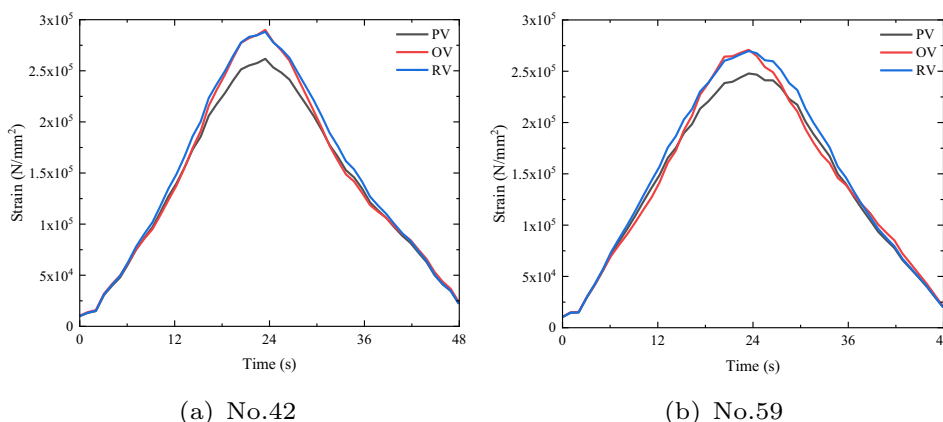
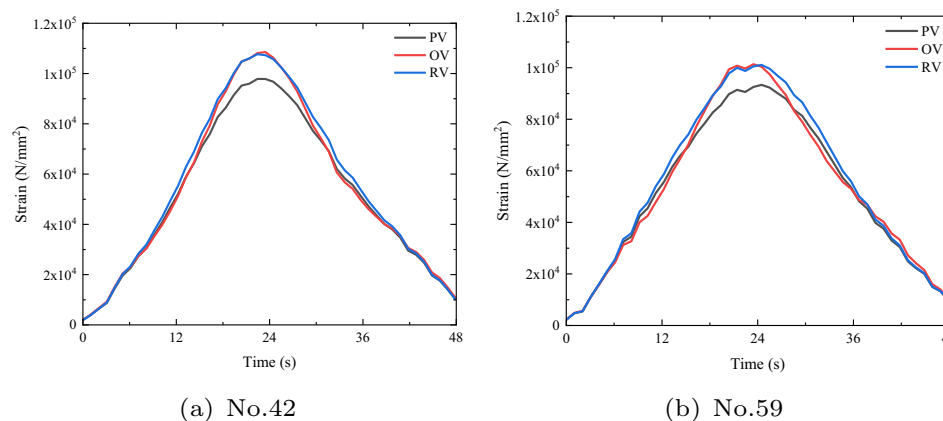


Fig. 8 Comparison the measuring point response considering the vehicle speed condition



exhibiting higher values of error. However, the coincidence between the OV curve and RV curve for each verification point is higher compared to the PV curve. The results shown in Fig. 10 are generally consistent, except for a few prominent points, with the highest level of agreement at the peak. This demonstrates the effectiveness of the proposed response reconstruction method. To further analyze the errors, the maximum response values of other measuring points are compared in each working condition, and the error graphs of the measuring points are obtained, as shown in Fig. 11.

In Fig. 11, only 8 points have a relative error between the PV curve and RV curve below 3%, while the remaining points

have errors above 6%, with a maximum error exceeding 10%. Through the proposed response reconstruction method, the relative errors between the OV curve and RV curve for all points are below 3%, with only a few points showing higher errors compared to the relative errors between the PV curve and RV curve. Among them, the maximum error is 2.3862%, while the minimum error is 0.0028%.

Considering the condition of vehicle speed and complex load conditions, the error between different methods is present, as depicted in Fig. 12. The relative error between the PV curve and RV curve is below 3%, while the remaining measuring points have larger errors, with a maximum

Fig. 9 Multi-lane moving load layout

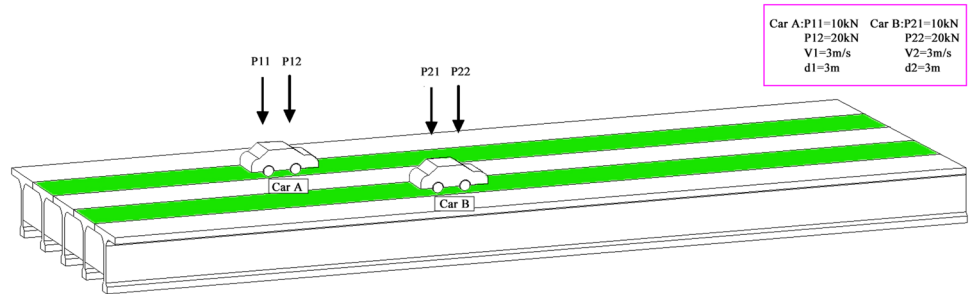
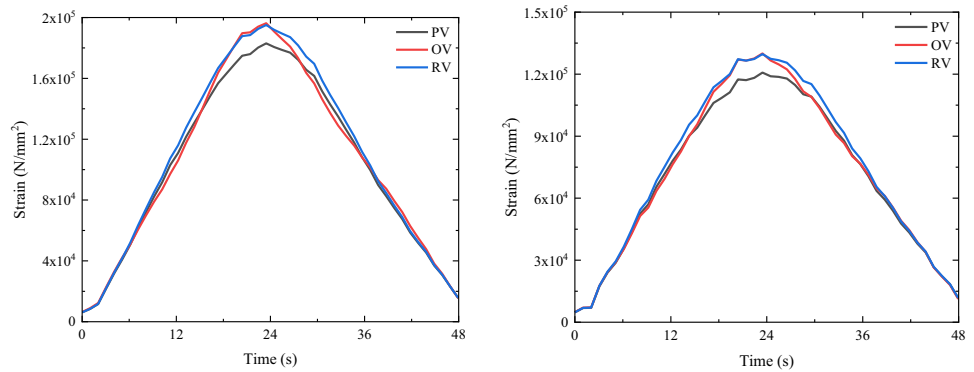


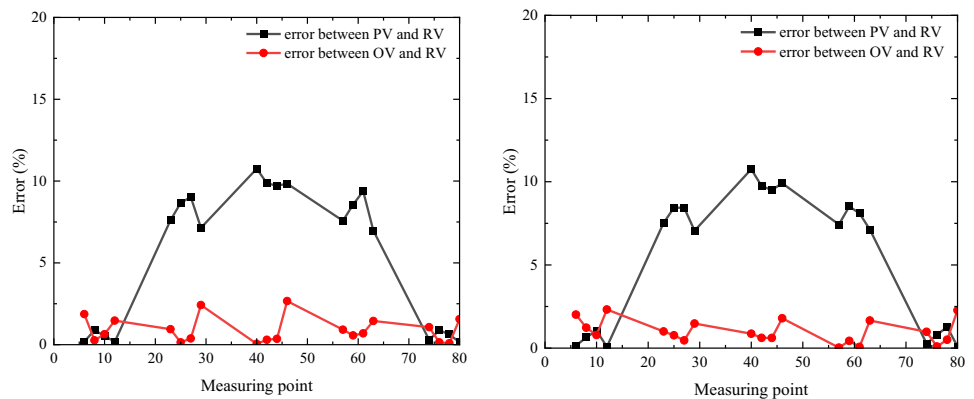
Fig. 10 Comparison of the measuring point response under complex load conditions



(a) No.42

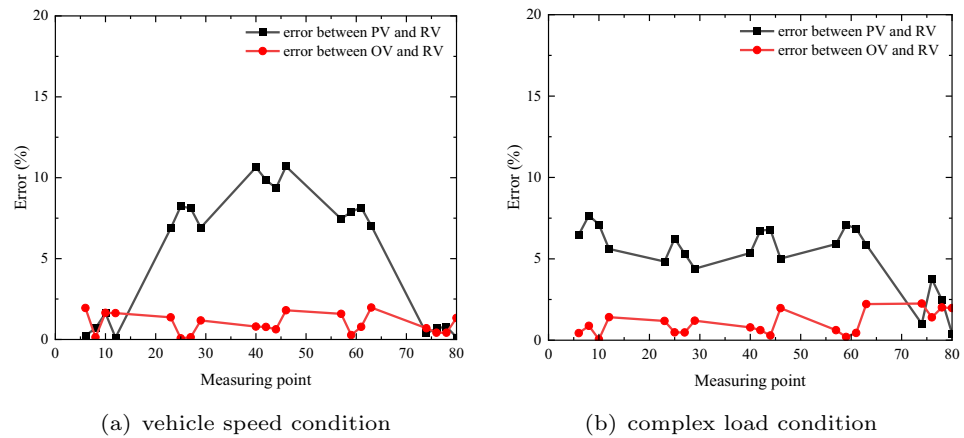
(b) No.59

Fig. 11 Errors of the measuring points under different working conditions



(a) standard working condition

(b) heavy working condition

Fig. 12 Errors of measuring points under different conditions

exceeding 6%. In addition, the relative errors between the OV curve and RV curve, identified by the proposed response reconstruction method, are all below 3%, with only a few points having higher errors than the relative errors between the PV curve and RV curve. Among them, the maximum error is 2.5787%, and the minimum error is 0.1758%.

Based on the tests conducted, various potential parameters have been considered and it was observed that the proposed response reconstruction method accurately identifies the OV curve of the measuring points. This curve exhibits a high level of consistency with the RV curve, indicating that the method is robust and unaffected by vehicle weight, speed, and complex load conditions. Consequently, the method can be regarded as accurate and reliable.

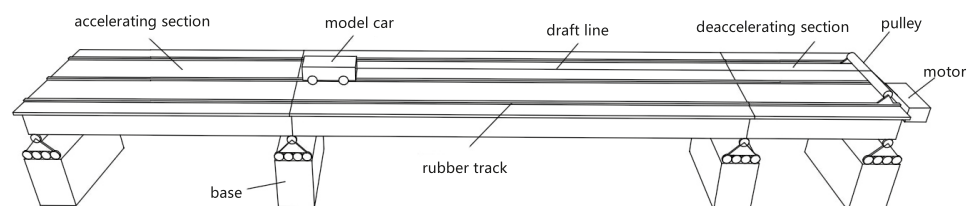
Experimental Verification

Setup of the Experimental

The response reconstruction theory has been validated in a finite-element model in “[Model Introduction](#)”, and to further confirm its validity, an isometric scale model of the actual bridge has been created in the laboratory. The actual bridge is constructed with concrete grade C55, and its single T-beam has a cross-sectional area of 1.313 m² and a cross-sectional moment of inertia $I_y = 1.23\text{m}^4$. In addition,

the bridge has a transverse width of 13.2 m, with a 1 m wide pavement and parapet on both sides, and a beam height of 2.75 m. The distance from the neutral axis to the top surface of the T-shape beam is 1.796 m, and to the bottom surface is 0.954 m. For the scaled-down model, various materials were considered, including micro-concrete, plaster, and plastic. Plexiglass is ultimately chosen due to its high transparency, ease of manufacturing, and ability to detect production defects. Furthermore, plexiglass is a durable material with a small modulus of elasticity, which reduces the weight of the model car and eases traction requirements during testing. Therefore, plexiglass is chosen to produce a scaled-down model of the real bridge, featuring an equal scale T-shaped simply supported beam.

Based on geometric similarity analysis, the researchers determined the scale of the organic-glass model bridge to be 20:1, with dimensions of 2.4 m in length, 0.66 m in width, and 0.1375 m in height. To maintain consistency with the actual bridge, the model includes five cross partitions with a thickness of 0.01 m, positioned approximately 0.106 m away from the bottom plate of the T-shaped beam flange. In addition, to achieve the desired speed of the model car on the bridge, acceleration and deceleration sections are set up before and after the main bridge, with lengths of 5 m and 2 m, respectively. The speed of the model car is ensured using a motor. Figure 13 illustrates the overall layout of the test system. During the test, a long-scale fiber-optic sensor is attached to the bottom of the model bridge to collect data, as shown in Fig. 14.

Fig. 13 Layout diagram of the overall test system

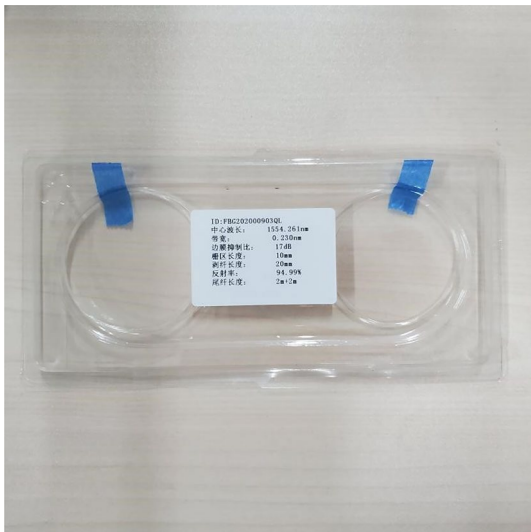


Fig. 14 The long-gauge FBG sensor

The Chinese road code [43] mandates that highways display the speed limits for each lane, ranging from a maximum of 120 km/h to a minimum of 60 km/h. To determine the model car speeds corresponding to actual speeds of 100 km/h, 80 km/h, and 60 km/h, dimensional analysis is employed, considering the speed similarity constants of the vehicles. Consequently, the model car speeds are 1.4 m/s, 1.12 m/s, and 0.84 m/s, respectively.

The laboratory tests involve dividing the single main girder into 12 cells of 20 cm each, resulting in a total of 60 cells and 65 nodes for the entire bridge. For practical reasons, the width between the two wheel centers of the test car is measured to be 18.5 cm. This bridge deck is set at 22 cm for each lane, allowing a gap of 1–2 cm on either side of the vehicle. During the single vehicle loading tests, the model car was positioned and driven in the middle lane. The sensor attachment area is chosen to be within 80–180 cm from

the approach end of the bridge, with the center point of the first column of sensors located at 90 cm from the approach end. A total of 25 sensors are arranged for the entire bridge, with 15 sensors collecting data for the known points and the remaining 10 sensors collecting data for the comparison of the calculation results, as shown in Fig. 15. The verification points are labeled A~J and the known points are denoted as S1~S15.

The experimental setup includes two prototype cars: a two-axle car and a three-axle car. The two-axle car has a weight of approximately 4.3 tonnes and an axle distance of 5 m. In contrast, the three-axle car weighs about 7 tonnes, with the front wheels positioned 3.46 m away from the middle axle, and the middle axle located 4.04 m from the rear axle. The test car configuration is depicted in Fig. 16. Car A represents the two-axle car, measuring 365 mm in length, 185 mm in width, and weighing 19.3 kg. Car B corresponds to the three-axle car, with dimensions of 500 mm in length, 185 mm in width, and a weight of 15.5 kg.

The experiment included the evaluation of a single model car and two model cars under different weight and speed conditions. The standard case, referred to as case 1, involved model car A with a weight of 19.3 kg, moving with the speed of 1.12 m/s on the bridge. Weight adjustments are made in Case 2, while speed adjustments were implemented in Case



Fig. 16 The model car A (two axles)

Fig. 15 Sensor layout diagram

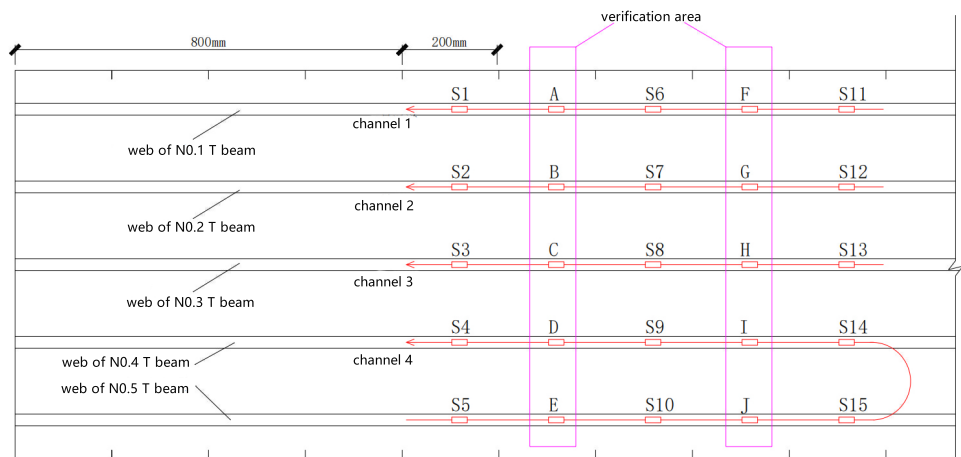


Table 1 Configuration of different cases

	Case1	Case2	Case3	Case4
Two-axis model car (Car A)				
Weight (kg)	19.30	27.70	19.30	19.30
Speed (m/s)	1.12	1.12	1.40	1.12
Three-axis model car (Car B)				
Weight (kg)	–	–	–	15.50
Speed (m/s)	–	–	–	1.12

3 for model car A. Case 4 represented a complex scenario where both model cars A and B are simultaneously driven on the road. As for the velocity with the motor, the speed of the model car in the finite element is converted to the test trolley speed by the speed similar constant of the vehicle, as shown in Eq. (29):

$$v_m = v_r \times l_m / l_r \tag{29}$$

where v_m is speed of the test trolley; v_r is the speed of the finite-element simulated vehicle; l_m is the test bridge length; l_r is the length of the finite-element bridge model.

After the speed of the test trolley is known, the motor frequency is obtained according to the conversion formula of motor frequency and vehicle speed. During the test, the frequency on the motor is adjusted to the corresponding value to obtain the ideal vehicle speed. The conversion formula of motor frequency is

$$F = v / (l \times 0.5) \tag{30}$$

where F is the motor frequency; v is the car speed; l is the perimeter of the rotating shaft. The specific weight and speed conditions for each case can be found in Table 1. Multiple tests are conducted for each condition, and a set of stable conditions is selected for further verification.

Analysis of Test Results

Prior to commencing the test, adjustments are made to the parameters such as sensor amplitude and frequency in the data acquisition software to ensure clear data visualization. The test officially commences when no alarms are triggered on the sensor interfaces and the standard deviation (STD) value meets the required stability criteria. Once the

Fig. 17 The stress response for different methods and cases

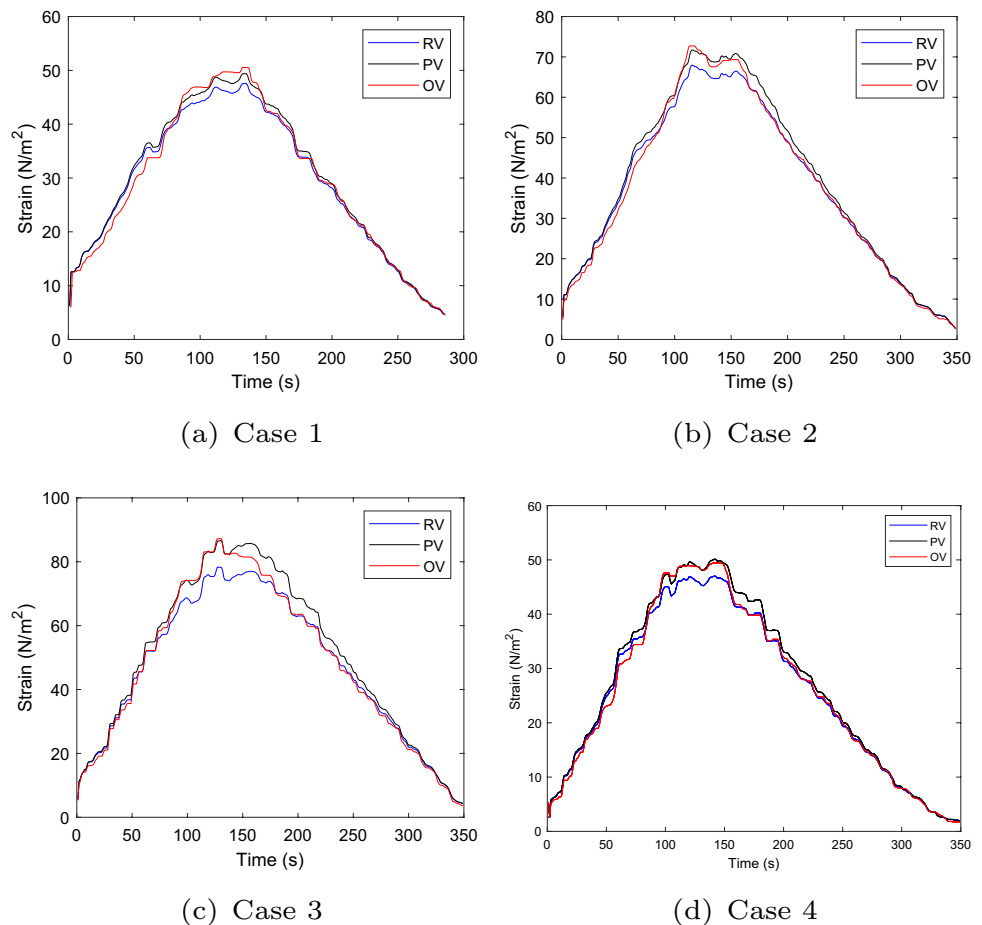
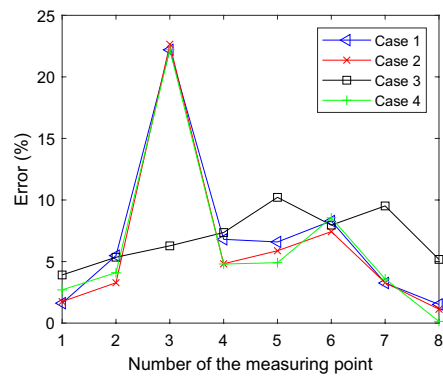
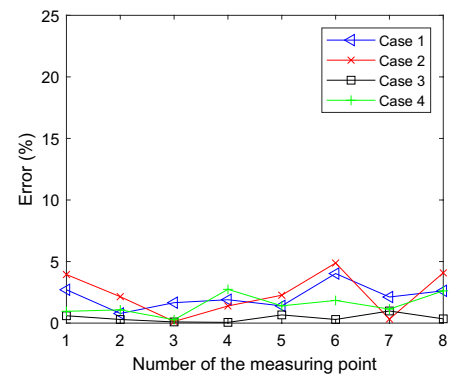


Fig. 18 The error for different working conditions



(a) Error between the maximum value of OV and RV



(b) Error between the maximum value of PV and RV

acquisition software initiates, the motor and vehicle are set in motion, and data collection concludes when the model car exits the bridge and the STD value stabilizes. Subsequently, the collected data is subjected to filtering and other necessary operations, enabling the calculation of predicted stress response values at all validation points. A comparison of the predicted values (PV), optimum values (OV), and real values (RV) for the four cases at validation point S4 is depicted in Fig. 17.

Comparing the results of the four cases at the same validation point, errors are observed between the predicted and actual PV curve for strain response, particularly at the peak. However, the overall trend between the OV curve and the RV curve remains consistent, and the error at the peak is significantly smaller compared to the error between the PV curve and the RV curve. Hence, the proposed method effectively validates the response. Furthermore, the results exhibit relative consistency between the OV and PV curves at the same validation point across the four operating conditions. This indicates the proposed method's insensitivity to factors such as weight, movement speed, and complex loading effects, further affirming its effectiveness. The maximum stress errors between OV and RV, PV and RV at the remaining validation points are depicted in Fig. 18.

As illustrated in Fig. 18, the results indicating that the maximum errors between the OV and RV curves are consistently below 5%. Although the maximum error between the PV and RV curves is typically below 5%, there are instances where it exceeds 10%. Apart from a few exceptions, the maximum error between the OV and RV curves is smaller than that between the PV and RV curves at all measurement points. These findings provide additional evidence supporting the effectiveness, accuracy, and validity of the proposed response reconstruction method, which remains unaffected by factors such as vehicle weight, speed, and complex loading effects.

Conclusions

In this paper, a response reconstruction method is introduced that combines the POD method, finite-element analysis to obtain the stress response of structural measuring points. It provides an overview of the fundamental principles of the eigen orthogonal decomposition method and explores the research on structural response reconstruction. In addition, it presents a sensor layout scheme and response reconstruction method utilizing the fusion force method and finite-element method. The effectiveness of the proposed method is validated by numerical simulations and laboratory tests, yielding the following key findings:

1. The proposed method underwent verification through numerical simulations, considering various factors such as vehicle speed, weight, and complex loads. The results demonstrate the accurate reconstruction of measuring point responses, highlighting the high precision of this method.
2. Verification of the proposed method was performed by numerical simulations and laboratory tests. Under different load conditions, including standard, vehicle speed, and vehicle weight, the error between the identified measuring point response and the actual response remained below 3%. This robust and effective method exhibits strong performance.
3. A flexible sensor layout scheme is introduced that can adapt to different scenarios, accommodating both convenient and challenging sensor arrangements within the target identification area. By employing a longitudinal measurement point mode and a time function, it becomes possible to separately identify a main beam measurement point and combine multiple main beams to assess response measurements in both vertical and horizontal bridge areas.

4. The laboratory experiment has been conducted using an isometric scaling model of the bridge, analyzing measurement data obtained from long-scale FBG sensors. The test results indicate that the maximum error between the identified point and its actual response time curve is less than 5%. Although the test point errors were slightly higher compared to the numerical simulations, it still remained within acceptable limits.

Acknowledgements We would like to express our gratitude to the following individuals for their contributions to this paper. Weimin Zhang for conceptualizing the research, conducting formal analysis, acquiring funding, and proposing the methods. Xiayi Zheng for the data curation, performing computational simulations, visualization, and analysis. Kan Liu for providing the initial draft writing, overseeing and editing the manuscript. Jian Chen for proofreading, project administration, and supervision. In addition, we would like to thank Jian Chen for his efforts in submitting and editing the manuscript. All the authors have reviewed and approved the final version of the manuscript.

Funding The Science and technology project of Zhejiang provincial water resource department (RC1945).

Data Availability All data, models, and code generated or used during this study are available upon request from the corresponding author.

Declarations

Conflict of Interest On behalf of all the authors, the corresponding author states that there is no conflict of interest.

References

- Li ZX, Hou GY, Hu JX (2021) Deformation monitoring of cracked concrete structures based on distributed optical fiber sensing technology. *Opt Fiber Technol* 61:102446
- Meng FY, Jia LM, Shen XH, Dong JW (2015) Research on application issues of structural health monitoring system based on optical fiber sensing technology. *Appl Mech Mater* 744:235–243
- Tang Y (2016) Concrete structure monitoring with distributed long-gauge optical fiber sensor. In: 2015 4th International Conference on Sensors, Measurement and Intelligent Materials (1124–1127). Atlantis Press
- Lian D (2021) Safety monitoring method of vehicle bridge stress structure based on wireless sensing technology. *J Phys: Conf Ser* 2029(1):012134
- Badia-Melis R, Ruiz-Garcia L, Garcia-Hierro J, Villalba JIR (2015) Refrigerated fruit storage monitoring combining two different wireless sensing technologies: RFID and WSN. *Sensors* 15(3):4781–4795
- He Z, Li W, Salehi H, Zhang H, Zhou H, Jiao P (2022) Integrated structural health monitoring in bridge engineering. *Automat Construct* 136:104168
- Kammer DC (1992) Effect of model error on sensor placement for on-orbit modal identification of large space structures. *J Guid Control Dynamics* 15(2):334–341
- Heo G, Wang ML, Satpathi D (1997) Optimal transducer placement for health monitoring of long span bridge. *Soil Dynam Earthq Eng* 16(7–8):495–502
- Flanigan CC, Botos CD (1992) Automated selection of accelerometer locations for modal survey tests. In: 10th International Modal Analysis Conference, 2:1205–1208
- Penny JET, Friswell MI, Garvey SD (1992) The automatic choice of measurement locations for dynamic testing. In: 10th International Modal Analysis Conference, 1:30–36
- Shi ZY, Law SS, Zhang LM (2000) Optimum sensor placement for structural damage detection. *J Eng Mech* 126(11):1173–1179
- MIN-SHUI HUANG, HONG-PING ZHU, JIN-QIANG SONG (2008) Application of Optimal Sensor Placement in Modal Parameters Test of Bridge Structure. *Journal of Highway and Transportation Research and Development* 2(143)
- Zhan L, Wu G, Li H, Chen S (2020) Synchronous identification of damage and vehicle load on simply supported bridges based on long-gauge fiber bragg grating sensors. *J Perform Construct Facilit* 34(1):04019097
- Zhang L, Wu G, Cheng X (2020) A rapid output-only damage detection method for highway bridges under a moving vehicle using long-gauge strain sensing and the fractal dimension. *Measurement* 158:107711
- Chen SZ, Wu G, Feng DC (2019) Damage detection of highway bridges based on long-gauge strain response under stochastic traffic flow. *Mech Syst Sig Proc* 127:551–572
- Zhang XH, Xu YL, Zhu S, Zhan S (2014) Dual-type sensor placement for multi-scale response reconstruction. *Mechatronics* 24(4):376–384
- Zhang XH, Zhu S, Xu YL, Homg XJ (2011) Integrated optimal placement of displacement transducers and strain gauges for better estimation of structural response. *Int J Struct Stab Dynam* 11(03):581–602
- Yang JN, Lei Y, Pan S, Huang N (2003) System identification of linear structures based on Hilbert-Huang spectral analysis. Part 1: normal modes. *Earthquake Eng Struct Dyn* 32(9):1443–1467
- Zou Y, Lu X, Yang J, Wang T, He X (2022) Structural damage identification based on transmissibility in time domain. *Sensors* 22(1):393
- Li J, Law SS (2012) Substructural damage detection with incomplete information of the structure
- Wang J, Yang Q (2016) Dynamic response reconstruction method in time domain based on state space. *J Build Struct* 37:460–6
- Kammer DC (1997) Estimation of structural response using remote sensor locations. *J Guid Control Dynam* 20(3):501–508
- He J, Guan X, Liu Y (2012) Structural response reconstruction based on empirical mode decomposition in time domain. *Mech Syst Sig Process* 28:348–366
- Huang NE, Shen Z, Long SR (1999) A new view of nonlinear water waves: the Hilbert spectrum. *Annual Rev Fluid Mech* 31:417–457
- Huang NE (2014) Hilbert-Huang transform and its applications, vol 16. World Scientific
- Huang NE, Shen Z, Long SR, Wu MC, Shih HH, Zheng Q, Liu HH (1998) The empirical mode decomposition and the Hilbert spectrum for nonlinear and non-stationary time series analysis. *Proc Royal Soc London. Series A: Mathemat Phys Eng Sci* 454(1971):903–995
- Ribeiro AMR, Silva JMM, Maia NMM (2000) On the generalisation of the transmissibility concept. *Mech Syst Sig Proc* 14(1):29–35
- Law SS, Li J, Ding Y (2011) Structural response reconstruction with transmissibility concept in frequency domain. *Mech Syst Sig Proc* 25(3):952–968
- Wang J, Law SS, Yang QS (2014) Sensor placement method for dynamic response reconstruction. *J Sound Vibrat* 333(9):2469–2482

30. Ma X, Vakakis AF, Bergman LA (2001) Karhunen-Loeve modes of a truss: transient response reconstruction and experimental verification. *AIAA J* 39(4):687–696
31. Bienkiewicz B, Tamura Y, Ham HJ, Ueda H, Hibi K (1995) Proper orthogonal decomposition and reconstruction of multi-channel roof pressure. *J Wind Eng Ind Aerodyn* 54:369–381
32. Ni ZH, Jiang ZR, Xie ZN (2007) POD technique and its application to prediction of wind pressure fields on roof. *J Vibrot Eng* 20(1):1–8
33. Jiang ZR, Ni ZH, Xie ZN (2007) Reconstruction and prediction of wind pressure field on roof. *Chin J Appl Mech* 20(1):592–598
34. Loeve M (2017) *Probability theory*. Courier Dover Publications
35. Davenport AG (1995) How can we simplify and generalize wind loads? *J Wind Eng Ind Aerodyna* 54:657–669
36. Ricciardelli F, de Grenet ET (2002) Analysis of the wind loading of a bridge deck box section using proper orthogonal decomposition. *International Journal of Fluid Mechanics Research* 29(3-4)
37. Liu Z, Liu Z, He C, Lu H (2019) Dimension-reduced probabilistic approach of 3-D wind field for wind-induced response analysis of transmission tower. *J Wind Eng Ind Aerodyn* 190:309–321
38. Wang H, Li W, Qian Z, Wang G (2021) Reconstruction of wind pressure fields on cooling towers by radial basis function and comparisons with other methods. *J Wind Eng Ind Aerodyn* 208:104450
39. Su Y, Di J, Li J, Xia F (2022) Wind pressure field reconstruction and prediction of large-span roof structure with folded-plate type based on proper orthogonal decomposition. *Appl Sci* 12(17):8430
40. Ma K, Hu C, Zhou Z (2019) Investigation on vortex-induced vibration of twin rectangular 5: 1 cylinders through wind tunnel tests and POD analysis. *J Wind Eng Ind Aerodyn* 187:97–107
41. Fang FX, Navon IM, Pain CC (2021) *Applications of efficient POD model order reduction to direct and inverse problems of fluid dynamics*, 1st edn. Chapman and Hall press
42. Li B, Gong CL, Su H (2017) Research and application on proper orthogonal decomposition in aerodynamic optimization of airfoil. *Aeros Shanghai* 34(5):117–123
43. State Council of the People's Republic of China (2017) *Regulations for the Implementation of the Road Traffic Safety Law of the People's 631 Republic of China*

Publisher's Note Springer Nature remains neutral with regard to jurisdictional claims in published maps and institutional affiliations.

Springer Nature or its licensor (e.g. a society or other partner) holds exclusive rights to this article under a publishing agreement with the author(s) or other rightsholder(s); author self-archiving of the accepted manuscript version of this article is solely governed by the terms of such publishing agreement and applicable law.